Study on wave-induced kinematic responses and flexures of ice floe by Smoothed Particle Hydrodynamics

Ningbo Zhang[1], Xing Zheng[1,*], Qingwei Ma[2,1]

[1] College of Shipbuilding Engineering, Harbin Engineering University, Harbin 150001, China
[2] School of Mathematics, Computer Science and Engineering, City University of London, London EC1V 0HB, UK

* Correspondence: zhengxing@hrbeu.edu.cn

Abstract

In this paper, a Smoothed Particle Hydrodynamics (SPH) method is extended to simulate the wave-ice interactions. The main contribution of this work is that an improved fluid-ice interface treatment scheme is included into SPH code to deal with the contact between the fluid and ice particles. The proposed SPH approach is applied to model two typical patterns of the wave-ice interaction process: the kinematic response of a small ice floe and the flexural motion of a sea ice floe, induced by water waves. To verify the accuracy of SPH method for the wave-ice interactions, the numerical results of SPH are compared with corresponding experimental data. The good agreement between the two demonstrates that the SPH method can be a useful numerical tool for simulating the wave-induced motion and bending deformation of an ice floe.

Keywords: SPH; wave-ice interaction; ice floe; kinematic response; wave-induced flexure; fluid-ice interface

1. Introduction

With the climate changes, the ice-covered seas are increasing in the cold ocean regions (Stephenson et al., 2011). Large-amplitude ocean waves are also becoming a common feature in the ice-covered ocean regions (Francis et al., 2011). There is growing observational and modeling evidence that the wave-ice interactions play an important role in these areas (Squire, 2007; Williams et al., 2013, Kohout et al., 2016). Therefore, there is a great need to understand the mechanics of wave-ice interaction, especially the wave-induced kinematic responses and flexures of the ice

floe. As it is a fundamental issue of the wave-driven impact of sea ice floes on offshore structure and it should be helpful to investigate the interactions between the water wave and sea ice, which could result in the breakup of ice into smaller floes.

The ice floes especially some small ones on the Marginal Ice Zone (MIZ), are sensitive to the motion driven by the ocean waves. The wave-driven floating ice floes can easily collide with the sea structure (Timco, 2011). So it is of great importance to study the kinematic responses of the small ice floes in waves, which are crucial to the understanding and mitigation of the potential hazard in the field (Mcgovern and Bai, 2014). In addition, the ocean waves can also cause ice floes to bend and flex. When the flexural motion is large enough, the ice floes can even break-up into many smaller segments. These fragmented floes are easier to be driven by ocean waves and melt (Steele, 1992). Thus, the wave-induced flexure of an ice floe plays a key role in the extent and strength of the ice cover.

In the past few years, some model tests of the wave-ice interaction have been conducted. Mcgovern and Bai (2014) made an experimental study on the kinematics of sea ice floes in regular waves. Meylan et al. (2015) used an experimental model to study the wave-induced flexure of a sea ice floe. An experimental model of transmission of the ocean waves by an ice floe was also presented by Bennetts et al. (2015), while another experimental investigation on the wave attenuation by a single ice floe in wave flume was carried out by Toffol et al. (2015).

In addition, many numerical models were also used to study the interaction of the wave and the ice. Sakai and Hanai (2002) used an empirical equation to study the celerity characteristics of wave that propagates in a model sea area covered with ice. Kohout and Meylan (2008) proposed a model based on the two-dimensional multiple floating elastic plate solution in the frequency domain to analyze the wave attenuation in the MIZ. Meylan et al. (2015) presented a theoretical model by using the potential flow and thin-plate theories to model flexural motion induced by the ocean waves. Bai et al. (2017) investigated the kinematic responses of small ice floe in regular waves by using the linear analysis based on the potential flow model and the CFD based on the viscous flow model separately. Williams et al. (2013) used a theoretical model of the wave-induced flexural motion to parameterize ice floe breakup. Besides, Montiel and Squire (2017) proposed a numerical model to investigate the ice floe breakup under ocean wave forcing in the MIZ. Skene et al. (2015) and Skene et al. (2018) have investigated the overwash and flexure of a thin floating plate and overwash of a step forced by regular incident waves, respectively, which is similar to the overwash and

flexure of an ice floe in the wave fields.

In recent years, the mesh-free approach, i.e. Smoothed Particle Hydrodynamics (SPH) method, is emerging as a potential tool for simulating the fluid flows and their interactions with highly deformable structures. SPH method has been widely applied to the computational fluid simulations which include weakly compressible fluid flows (Morris et al., 1997), strictly incompressible fluid flows (Shao and Lo, 2003; Shao, 2010), water wave dynamics (Khayyer et al., 2008; Zheng et al., 2014) and etc. On the other hand, the SPH method has also been employed in quite a few solid mechanics problems. For example, it was first used by Libersky and Petschek (1991) and then by Randles and Libersky (1996) for the investigations of large deformation and corresponding response of a solid material. Zhang et al. (2017) applied the SPH method to study the bending and compression failure progress of the ice. The SPH method has also received some attentions in the fluid-solid interaction problems. Bui et al. (2007) introduced an algorithm to simulate the interactions between the water and the soil. By using the SPH algorithm, Antoci et al. (2006, 2007) studied the complex hydroelastic problems and Amini et al. (2011) made investigations on the fluid-hypo-elastic solid interactions using SPH model. The hydroelastic problems were also simulated by He et al. (2017) using a coupled weakly compressible and total Lagrangian (WC-TL) SPH method.

In this paper, the SPH method is extended to simulate wave-induced the kinematic responses and flexures of an ice floe. The main contributions of this paper lie in the following two aspects. On the one hand, a simple and effective interface treatment method for modeling the contact between the fluid and the ice floe is implemented in the SPH framework to simulate the wave-ice interactions. In this treatment, the ice particles from ice floe act as the dummy particles to approximate the interface between the fluid phase and the ice floe. The resulting forces on the ice particles from the fluid are derived based on the momentum balance and obtained by the volume integration of the fluid stresses of the neighboring fluid particles in the support area. Because there is no need to calculate the geometry of the ice floe boundary and the interface surface, this method provides a natural coupling treatment for the interaction between the fluid and ice particles, which is easy to implement even with complex geometries for ice floe in more complex and practical wave-ice interaction problems. On the other hand, the above literature reviews indicated that it is relatively challenging to simulate the kinematic responses and flexures by using the same numerical model. During the practical process of the wave-ice interaction, however,

both the dynamic movement and bending deformation of the ice floe essentially occur together. This underlines the importance of simulating these two common processes in wave-ice interaction problems with a unified model.

The present paper is structured as follows: Firstly, the governing equations of SPH are briefly introduced, for both the fluid and the solid phases. Secondly, some key numerical techniques are reviewed in Section 3, which includes the spatial derivative approximation of various SPH interaction terms, the imposition of Simplified Finite Difference Interpolation (SFDI) scheme, and the selections of computational time step and boundary conditions. Then the details of the fluid-solid interaction algorithm are developed in Section 4. Finally, the proposed SPH method is applied to simulate the kinematic response of an ice floe in regular waves and the wave-induced flexure of a sea ice floe, and validated against the experimental results. The satisfactory performance of the model in dealing with the complex wave-ice interactions is fully demonstrated by the comparisons with experimental data.

2. Governing equations

The governing equations in a SPH method are the mass and momentum conservation equations written in the Lagrangian form, based on the Navier-Stokes equations.

$$\frac{D\rho}{Dt} = -\rho \frac{\partial v^{\alpha}}{\partial x^{\alpha}} \tag{1}$$

$$\frac{Dv^{\alpha}}{Dt} = \frac{1}{\rho} \frac{\partial \sigma^{\alpha\beta}}{\partial x^{\beta}} + g^{\alpha} \tag{2}$$

where α and β indicate the Cartesian components in x and y directions; ρ, v and $\sigma^{\alpha\beta}$ are the particle density, velocity and stress tensor, respectively; g is the gravitational acceleration; D/Dt denotes the particle derivative.

The stress tensor can be decomposed into two parts, which are the hydrostatic pressure and deviatoric shear stress:

$$\sigma^{\alpha\beta} = -p\delta^{\alpha\beta} + s^{\alpha\beta} \tag{3}$$

in which $\delta^{\alpha\beta}$ is Kronecker delta and $\delta^{\alpha\beta} = 1$ if $\alpha = \beta$ or $\delta^{\alpha\beta} = 0$ when $\alpha \neq \beta$.

2.1. Fluid flow equations

The mass conservation equation for the fluid is shown as Eq. (1). It assumes the fluid to be weakly-compressible and non-viscous. The momentum conservation equation for fluid is written as:

$$\frac{Dv^{\alpha}}{Dt} = -\frac{1}{\rho}\frac{\partial p}{\partial x^{\alpha}} + g^{\alpha} \tag{4}$$

In order to simulate a weakly compressible fluid, the following equation of state (EOS) is used which defines the relation among the pressure, density and sound speed:

$$p = B\left[\left(\frac{\rho}{\rho_0}\right)^{\gamma} - 1\right] \tag{5}$$

where $\gamma = 7$ and $B = \frac{c_f^2 \rho_0}{\gamma}$, ρ_0 is the reference density, c_f is the reference sound speed for the fluid. c_f =10$u_{\max}$ is adopted in this paper and $u_{\max}$ is the maximum flow velocity.

2.2. Solid equations

Governing equations for the ice particles are the same as Eqs. (1) and (2). Similar to Zhang et al. (2017), the hydrostatic pressure p for ice particles in Eq. (3) is defined by using the mean stress, which means $p = -\sigma^{\gamma\gamma}/3$ in this paper. The stress tensor can be written as follows:

$$\sigma^{\alpha\beta} = \frac{1}{3}\sigma^{\gamma\gamma}\delta^{\alpha\beta} + s^{\alpha\beta} \tag{6}$$

The ice floe is conducted as an elastic material based on Sergienko (2010). The elastic strain rate tensor $\dot{\varepsilon}^{\alpha\beta}$ normally follows the generalized Hooke's law:

$$\dot{\varepsilon}^{\alpha\beta} = \frac{\dot{s}^{\alpha\beta}}{2G} + \frac{1-2\upsilon}{3E}\dot{\sigma}^{\gamma\gamma}\delta^{\alpha\beta} \tag{7}$$

in which $\dot{s}^{\alpha\beta}$ is the deviatoric shear stress rate tensor; G and E are the shear modulus and Young's modulus, respectively; υ is the Poisson's ratio.

In order to take the superposed rigid rotation into account for the constitutive

relations, the Jaumann stress rate is adopted when involving the large deformation. As a result, the final form of the stress-strain relationship of the elastic ice material can be shown as

$$\dot{\sigma}^{\alpha\beta} = 2G\dot{e}^{\alpha\beta} + K\dot{\varepsilon}^{\alpha\beta}\delta^{\alpha\beta} + \sigma^{\alpha\gamma}\dot{\omega}^{\beta\gamma} + \sigma^{\gamma\beta}\dot{\omega}^{\alpha\gamma} \tag{8}$$

in which α and β denote the Cartesian components in x and y directions, respectively; $\dot{e}^{\alpha\beta} = \dot{\varepsilon}^{\alpha\beta} - \frac{1}{3}\dot{\varepsilon}^{\gamma\gamma}\delta^{\alpha\beta}$ is the deviatoric shear strain rate tensor, $G = E/(2(1+\upsilon))$ is the shear modulus, $K = E/(3(1-2\upsilon))$ is the elastic bulk modulus. The components of the strain rate $\dot{\varepsilon}^{\alpha\beta}$ are given by:

$$\dot{\varepsilon}^{\alpha\beta} = \frac{1}{2}\left(\frac{\partial v^{\alpha}}{\partial x^{\beta}} + \frac{\partial v^{\beta}}{\partial x^{\alpha}}\right) \tag{9}$$

and $\dot{\omega}^{\alpha\beta}$ is the rotation rate tensors defined as:

$$\dot{\omega}^{\alpha\beta} = \frac{1}{2}\left(\frac{\partial v^{\alpha}}{\partial x^{\beta}} - \frac{\partial v^{\beta}}{\partial x^{\alpha}}\right) \tag{10}$$

3. SPH formulations

3.1.Spatial derivatives and particle approximation in SPH

In the SPH method, the quantities of particle i can be approximated by the direct summation of the relevant quantities of its neighbouring particles j. Following the study of Colagrossi et al. (2009) and Adami et al. (2012), the continuity Eq. (1) can be approximated as follows:

$$\frac{D\rho_i}{Dt} = m_i \sum_{j=1}^{N} \frac{m_j}{\rho_j}\left(v_i^{\alpha} - v_j^{\alpha}\right)\frac{\partial W_{ij}}{\partial x_i^{\alpha}} \tag{11}$$

where ρ_i and m_i are the density and mass of particle i with velocity component v_i; ρ_j and m_j are the density and mass of particle j which has velocity component v_j. A proper artificial diffusive term based on Antuono et al. (2010) is adopted into the continuity equation, which can remove the spurious high-frequency oscillations in the pressure field for the fluid simulation. This δ-*SPH* scheme reads:

$$\frac{D\rho_i}{Dt} = \sum_{j=1}^{N} m_j\left(v_i^{\alpha} - v_j^{\alpha}\right)\frac{\partial W_{ij}}{\partial x_i^{\alpha}} + \delta h c_0 \sum \psi_{ij} \cdot \frac{\partial W_{ij}}{\partial x_i^{\alpha}} V_j \tag{12}$$

where

$$\psi_{ij} = 2\left(\rho_j - \rho_i\right)\frac{\boldsymbol{r}_{ji}}{\left|\boldsymbol{r}_{ij}\right|^2} - \left[\left\langle\nabla\rho\right\rangle_i^L + \left\langle\nabla\rho\right\rangle_j^L\right] \tag{13}$$

$$\left\langle\nabla\rho\right\rangle_i^L = \sum_j\left(\rho_j - \rho_i\right)\boldsymbol{L}_i\nabla_i dV_j \tag{14}$$

$$\boldsymbol{L}_i = \left[\sum_j\left(r_j - r_i\right)\otimes\nabla_i W_{ij}dV_j\right]^{-1} \tag{15}$$

and $\boldsymbol{r}_{ji} = \boldsymbol{r}_j - \boldsymbol{r}_i$. The coefficient δ controls the order of magnitude of the diffusive term and is set to be 0.01 in this paper.

According to Colagrossi et al. (2009), in which the free surface effect is considered, the SPH approximation of the momentum equation for the fluid can be written as:

$$\frac{dv_i^\alpha}{dt} = \sum_{j=1}^N m_j\left(-\frac{p_i + p_j}{\rho_i\rho_j} - \Pi_{ij}\right)\frac{\partial W_{ij}}{\partial x_i^\alpha} + g^\alpha \tag{16}$$

where Π_{ij} is the artificial viscosity, which was proposed by Monaghan (1992).

In this paper, an artificial stress method proposed by Monaghan (2000) and Gray et al. (2001) is adopted to remove the numerical instability (Swegle et al., 1995), which is caused by clumping of the SPH particles for the solid mechnamics. The SPH approximation of the momentum equation for the ice model is shown as

$$\frac{dv_i^\alpha}{dt} = \sum_{j=1}^N m_j\left(\frac{\sigma_i^{\alpha\beta}}{\rho_i^2} + \frac{\sigma_j^{\alpha\beta}}{\rho_j^2} - \Pi_{ij}\cdot\delta^{\alpha\beta} + f_{ij}^n\left(R_i^{\alpha\beta} + R_j^{\alpha\beta}\right)\right)\frac{\partial W_{ij}}{\partial x_i^\beta} + g^\alpha \tag{17}$$

where $R_i^{\alpha\beta}$ and $R_j^{\alpha\beta}$ are the artificial stress tensor of particles i and j, respectively, with the correction parameter ε (Gray et al., 2001). For all tests discussed in this study, $\varepsilon = 0.3$ and $n = 4$ are adopted. f_{ij} is defined as $f_{ij} = W_{ij}/W\left(\Delta d, h\right)$, Δd is the initial distance between two neighbouring particles.

In this paper, the quintic kernel proposed by Wendland (1995) is used. In addition, the position of particle i is defined based on the XSPH method (Monaghan 1992), which is shown as

$$\frac{Dx_i^\alpha}{Dt} = v_i^\alpha + \bar{\varepsilon}\sum_{j=1}^N\frac{m_j}{\rho_j}\left(v_j^\alpha - v_i^\alpha\right)W_{ij}, \quad \bar{\varepsilon}\in\left[0,1\right] \tag{18}$$

3.2. SFDI method

The Simplified Finite Difference Interpolation (SFDI) method is applied to calculate the strain rate of the ice particles, more details about the SFDI method can be found in Ma (2011). The enhanced performance of the SFDI method in solid mechanics can be found in Zhang et al. (2017). The strain rate of the tensor calculated by the SFDI method in 2D case can be written as

$$\dot{\varepsilon}^{\alpha\beta} = \frac{1}{2}\left(\sum_{j=1,\, j\neq i}^{N} \frac{n_{i,\alpha} B_{ij,\beta} - n_{i,\beta} B_{ij,\alpha}}{n_{i,x} n_{i,y} - n_{i,\alpha\beta}^{2}} \left(v_j^{\alpha} - v_i^{\alpha} \right) + \sum_{j=1,\, j\neq i}^{N} \frac{n_{i,\beta} B_{ij,\alpha} - n_{i,\alpha} B_{ij,\beta}}{n_{i,x} n_{i,y} - n_{i,\alpha\beta}^{2}} \left(v_j^{\beta} - v_i^{\beta} \right) \right) \tag{19}$$

where $n_{i,m} = \sum_{j=1,\, j\neq i}^{N} \frac{(r_j^m - r_i^m)^2}{\left| \boldsymbol{r}_j - \boldsymbol{r}_i \right|^2} W\left(\boldsymbol{r}_{ij} \right)$, $n_{i,mk} = \sum_{j=1,\, j\neq i}^{N} \frac{(r_j^m - r_i^m)(r_j^k - r_i^k)}{\left| \boldsymbol{r}_j - \boldsymbol{r}_i \right|^2} W\left(\boldsymbol{r}_{ij} \right)$, $B_{ij,m} = \frac{(r_j^m - r_i^m)}{\left| \boldsymbol{r}_j - \boldsymbol{r}_i \right|^2} W\left(\boldsymbol{r}_{ij} \right)$, where $m = x$, $k = y$ or $m = y$, $k = x$, N is the number of neighboring particle for particle i, r_j^m indicates the component of the position vector of x or y direction.

3.3. Time step

To ensure the stability and accuracy of the integration scheme in solid and fluid solvers, the stepping length is governed by CFL-condition (Adami et al., 2012). The time step for the ice model is determined as

$$\Delta t_i \leq 0.3 \left(\frac{h_i}{c_i} \right) \tag{20}$$

where $c_i = \sqrt{\frac{K}{\rho_0}}$ is the sound speed for the ice, K is the bulk modulus, ρ_0 is the reference density of the ice.

The time step for the fluid model is shown as

$$\Delta t_f \leq 0.2 \cdot \min \left(\frac{h_f}{a_{\max}}, \frac{h_f}{c_f + u_{\max}} \right) \tag{21}$$

where $a_{\max}$ is the maximum acceleration, $u_{\max}$ is the maximum velocity.

It needs to be noted that the sound speed is obtained by using $c_f = 10 u_{\max}$, so its value depends on each different cases. During the numerical test of wave-ice interaction in section 5, the time step of the fluid phase is much larger than the one of the ice model. In order to balance the computation time of the fluid and ice model, the

time step of the fluid Δt_f is determined by $\Delta t_f = n\Delta t_i$, n is a constant, which is an integer multiple obtained from dividing the time step of the fluid in Eq. (21) by the one for the ice in Eq. (20).

3.4. Boundary conditions

In this part, the fixed solid boundary and the wavemaker boundary with the free-slip condition were modeled by using the mirror particles method following Randles and Libersky (1996). In the interaction zone between the fluid phase and the solid body, the solid particles represent the dummy particles, which can act on the continuity equation for the fluid phase. Thereby the density of a fluid particle contacted with the solid particles will increase which makes the pressure of this fluid particle positive. The positive pressure force obtained by these solid particles can prevent fluid particles from passing through solid particles. So the non-penetration impermeability condition on the boundary of solid body can be satisfied implicitly. In addition, according to Adami et al. (2012), the free-slip boundary condition can be applied on the solid body by simply neglecting the viscous interaction between fluid particles and adjacent solid particles.

4. Fluid-solid interaction scheme

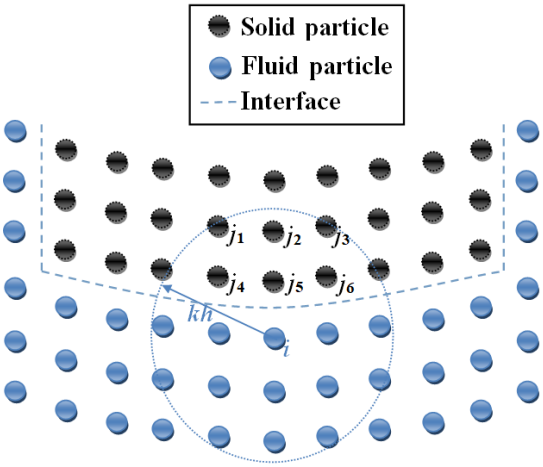

(a)

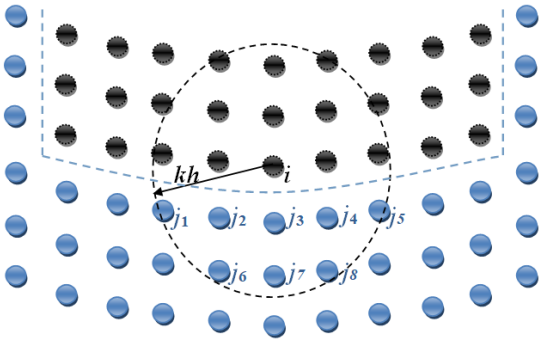

(b)

Fig. 1. A schematic of fluid and solid particles at interface boundary: (a) the scheme of the fluid particle i calculation; (b) the scheme of the solid particle i calculation.

During the wave–ice interaction simulation, the contact algorithm is of high importance on the interaction zone (**Fig. 1)**. In this study, a simple and effective wave-ice interface scheme is proposed. This new method introduces the dummy particles to approximate the interface between the fluid particles and the solid particles. When solving the equations of fluid mechanics, the solid particles in the neighbouring domain of the fluid particle i can act as the dummy particles for strengthening the boundary conditions. When solving the momentum equations of the fluid particle i which have both fluid and solid particles in its neighbor supporting domain, the solid particles j in the neighbouring domain of the fluid particle i (Fig. 1a) are taken into account in the calculation of the momentum equations:

$$\frac{dv_i^\alpha}{dt} = \sum_{j\in ice}^{N} m_j \left(-\frac{p_i + p_j}{\rho_i \rho_j} \right) \frac{\partial W_{ij}}{\partial x_i^\alpha} + \sum_{j\in fluid}^{N} m_j \left(-\frac{p_i + p_j}{\rho_i \rho_j} - \Pi_{ij} \right) \frac{\partial W_{ij}}{\partial x_i^\alpha} + g^\alpha \qquad (22)$$

When acting as dummy particles, the corresponding pressure of ice particle j in above equation can be interpolated by using the values of neighboring fluid particles by Eq. (23) which can refer to Adami et al. (2012).

$$p_j = \frac{\sum_{i\in fluid}^{M} p_i W_{ji} + (\mathbf{g} - \boldsymbol{a}_j) \cdot \sum_{i\in fluid}^{M} \rho_i \boldsymbol{r}_{ji} W_{ji}}{\sum_{i\in fluid}^{M} W_{ji}} \qquad (23)$$

The first item on the left hand in Eq. (22) is derived from the force over the solid particles acting on the fluid particles. When the solid particles act as the dummy

particles for the fluid, the approximations of the force on the solid particle i from the fluid particles are evaluated by using the volume integration of the fluid stresses tensor of its neighbouring fluid particles, which is also based on the momentum equation. According to Ren et al. (2015) where the wave-induced motions of a rigid body is considered, the force on solid particle i from its neighbouring fluid particles j (Fig. 1b) can be derived as

$$\boldsymbol{F}_{fluid-solid,i} = m_i \sum_{j\in fluid}^{N} m_j \left(-\frac{p_i + p_j}{\rho_i \rho_j} \right) \frac{\partial W_{ij}}{\partial x_i^{\beta}} \tag{24}$$

Correspondingly, the momentum equation of solid particle i in the interaction zone can be written as

$$\frac{dv_i^{\alpha}}{dt} = \sum_{j\in fluid}^{N} m_j \left(-\frac{p_i + p_j}{\rho_i \rho_j} \right) \frac{\partial W_{ij}}{\partial x_i^{\alpha}} + \sum_{j\in ice}^{M} m_j \left(\frac{\sigma_i^{\alpha\beta}}{\rho_i^2} + \frac{\sigma_j^{\alpha\beta}}{\rho_j^2} - \Pi_{ij} \cdot \delta^{\alpha\beta} \right) \frac{\partial W_{ij}}{\partial x_i^{\beta}} + g^{\alpha} \tag{25}$$

In the past few years, some FSI studies by using the SPH method have been conducted. Antoci et al. (2007) introduced the kinematic and dynamic interface conditions to model FSI problems considering a non-viscous flow by SPH. In addition, a repulsive force method was used to solve contact problems between the fluid and solid particles like Amini et al. (2011). Paredes and Imas (2013) also adopted a repulsive force method to model the coupling problems of fluid-structure interactions. Recently, He et al. (2017) used a coupled WC-TL SPH method to solve the hydroelastic problems. In their work, an equivalent interfacial force from fluid is applied to the solid body. Table.1 gives the short summary of these fluid–solid interaction schemes.

Tab.1 Summary of four different fluid–solid interaction schemes.

Schemes and references	Main formulations	Main features
Antoci et al. (2007)	$\boldsymbol{F}_{fluid-solid,s} = p_{\mathrm{int}_s} \int_{\Gamma} W\left(\left\|\boldsymbol{r}_{\mathrm{int}_s} - \boldsymbol{r}'\right\|, h\right) d\Gamma'$ $p_{\mathrm{int}_s} = 2\sum_{b\in\Omega_f} \frac{m_b}{\rho_b} p_b W\left(\left\|\boldsymbol{r}_{\mathrm{int}_a} - \boldsymbol{r}_b\right\|, h\right)$	The method needs to calculate the precise position of interface surface and its normal direction previously. Then a linear integration

	$\boldsymbol{r}_{\mathrm{int}_s} = \boldsymbol{r}_s + (a+\frac{1}{2})d\hat{\boldsymbol{n}}_s,$ $\hat{\boldsymbol{n}}_s = \left(-\frac{r_{s+1}^{\beta} - r_{s-1}^{\beta}}{\lvert \boldsymbol{r}_{s+1} - \boldsymbol{r}_{s-1} \rvert}, \frac{r_{s+1}^{\alpha} - r_{s-1}^{\alpha}}{\lvert \boldsymbol{r}_{s+1} - \boldsymbol{r}_{s-1} \rvert} \right)$ $\boldsymbol{F}_{solid-fluid,s^*} = -\boldsymbol{F}_{fluid-solid,s}$ where $\boldsymbol{r}_{\mathrm{int}_a}$ is the position of the interface point closest to each solid particle s, a is the number of rows between particle s and the boundary, $\hat{\boldsymbol{n}}_s$ is the normal unit vector of solid particle s, the subscripts s+1 and s-1 identify the particles preceding and following particle s.	needs to be performed on the boundary for each boundary particle. This method requires a lot of complicated calculation. Therefore, the fluid-solid interaction is difficult to achieve, especially in the case of complex boundaries.
Amini et al. (2011)	Repulsive force: $\boldsymbol{F}_{fs} = -\sum_s K_f \left(\frac{kh}{r_{fs} + \eta_1} \right)^{\eta_2} \frac{m_f m_s}{\rho_f \rho_s} p_f \boldsymbol{r}_{fs} W_{fs}$ where K_f , η_1, and η_2 are constants. kh is the radius of the kernel and r_{fs} is the distance between fluid and solid particles.	The parameters in calculation of the repulsive force are uncertainty, which will lead to the numerical complexity and instability.
Paredes and Imas (2013)	Repulsive force: $\boldsymbol{F}_{fs} = gH \frac{m_{skin} \cdot \beta}{\bar{m}_f} \frac{\boldsymbol{r}_{fs}}{r_{fs}^2} W_{fs}$ where $\beta = p_f / p_s$, m_{skin} is the mass of solid particle on the skin layer, $\bar{m}$ is the mass of a fluid particle	The ‘skin’ particle layer needs to be created to ‘wrap’ the solid. In addition, the uncertainty of repulsive force also leads to the inaccuracy and instability of the numerical results.
He et al. (2017)	$\boldsymbol{F}_{fluid-solid,s} = p_s \Delta r_s \hat{\boldsymbol{n}}_s$ $\Delta r_s = \frac{1}{2}\lvert \mathbf{r}_s - \mathbf{r}_{s-1} \rvert + \frac{1}{2}\lvert \mathbf{r}_{s+1} - \mathbf{r}_s \rvert$ where $\hat{\boldsymbol{n}}_s$ is the unit normal vector at interface solid particle s, s+1 and s-1 are adjacent interface solid particles of particle s.	This method needs to identify the interface particles on the outer layer of solid body and get their arrangement order, calculate their normal direction, which increase the difficulty and workload of the

		calculation.
Presented method	$\boldsymbol{F}_{fluid-solid,s} = m_s \sum_{j \in fuid}^{N} m_j \left(-\frac{p_s + p_j}{\rho_s \rho_j} \right) \frac{\partial W_{sj}}{\partial x_s^{\beta}}$ where p_s is the corresponding pressure of solid particle s acting as dummy particle and obtained by Eq.(23).	The presented method does not require explicit information about the geometry of the solid boundary and the interface surface, e.g. the position of interface surface particles and their normal vectors.

In this work, the main advantage of the proposed interface method is simple and convenient of calculation, since it does not require complex processes for identifying the solid boundary and calculating the interface surface parameters. Hence, it is easy to implement and suitable for modeling the complex cases of wave and ice coupling problems with irregular boundaries of ice floe. The numerical tests in section 5 show that this proposed interface scheme can get good results for simulating the wave-ice interaction problems effectively and accurately.

4.1. An elastic plate subjected time-dependent water pressure

In order to verify the feasibility of the presented SPH method for fluid-solid interaction mechanics, the elastic displacement of an elastic plate subjected time-dependent water pressure is conducted in this part, which includes the comparisons with different coupling schemes.

The elastic deformation of the plate subjected to water pressure is implemented, which is a benchmark test to verify the validity of the proposed interface treatment scheme for the case of fluid-solid interactions. The experimental and numerical study on elastic deformation of plate subjected to water pressure were conducted by Antoci et al. (2007). The initial calculation model is shown in **Fig. 2**. The elastic plate has the density $\rho = 1100$ kg/m^3, the elastic modulus $E = 2.0$ GPa and Poisson's ratio $\nu = 0.4$. In this case, an initial particle size $dx = 0.01$ m is adopted.

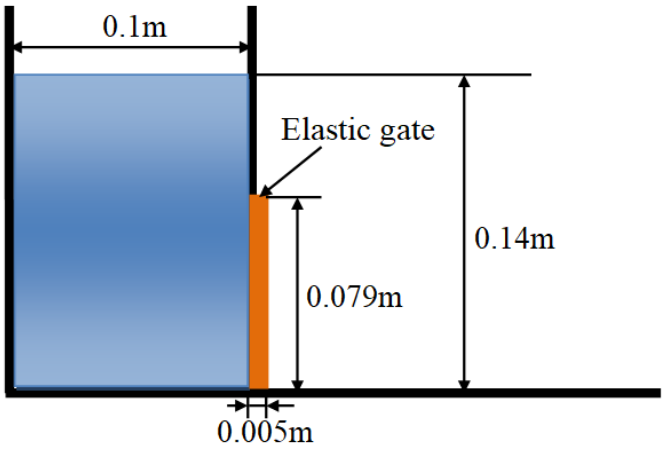

Fig. 2. The cantilever beam and the dynamic loads.

To quantify the numerical results, **Fig. 3** shows a series of the comparisons of the deformation process of elastic gate under water pressure. During the comparison, the experimental photographs are from Antoci et al. (2007). According to the results of **Fig. 3**, the free surface profile of overall flow field and the displacement of the elastic gate are similar to that on the corresponding experiment photos. In order to show the quality of this improvement, **Fig. 4** gives the comparison of the horizontal and vertical displacement of the free end of the elastic gate among present SPH results, other SPH results (Antoci et al., 2007; Amini et al., 2011; Paredes and Imas, 2013; He et al., 2017) and the experimental data. It shows that the time histories of the displacement obtained by the presented SPH method get a good agreement with the experimental data, although there exists some differences. But the presented results show better agreement with the experimental data compared with other SPH results.

Moreover, it gives an error analysis to test the accuracy of different numerical methods. The averaged errors of different methods are obtained by $Er_d = \sqrt{\sum_{i=1}^{N}(d-d_0)^2} \Big/ \sqrt{\sum_{i=1}^{N} d_0^{\,2}}$, where d is the displacement of numerical results above from $t = 0.0$ s to $t = 0.4$ s, d_0 is the corresponding displacement of experimental data from $t = 0.0$ s to $t = 0.4$ s. It shows that the relative errors are around 10.35% for the results in Antoci et al. (2007), 4.33% for that of Amini et al. (2011), 10.52% for that of Paredes and Imas (2013), 5.01% for that of He et al. (2017), and only 2.39% for that of the presented method, when compared with the experimental in **Fig. 4**(a). In the case of vertical displacement comparison, these errors are about 13.89%, 8.53%, 12.42%, 6.71% and 4.82%, respectively, which is shown in **Fig. 4**(b)**.** In general, the numerical results of the presented method can

achieve good accuracy in predicting the displacement at the free end of the elastic gate.

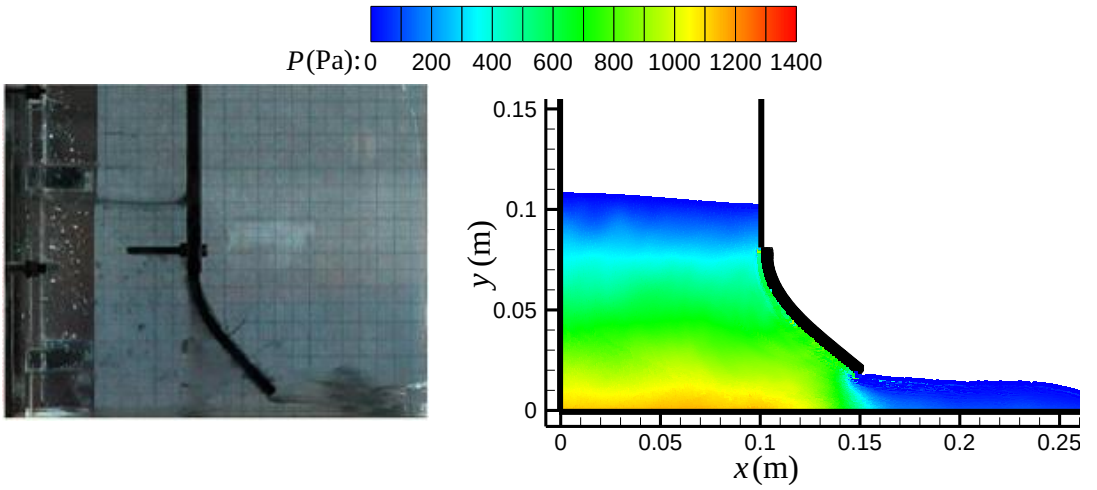

(a) $t = 0.178$ s

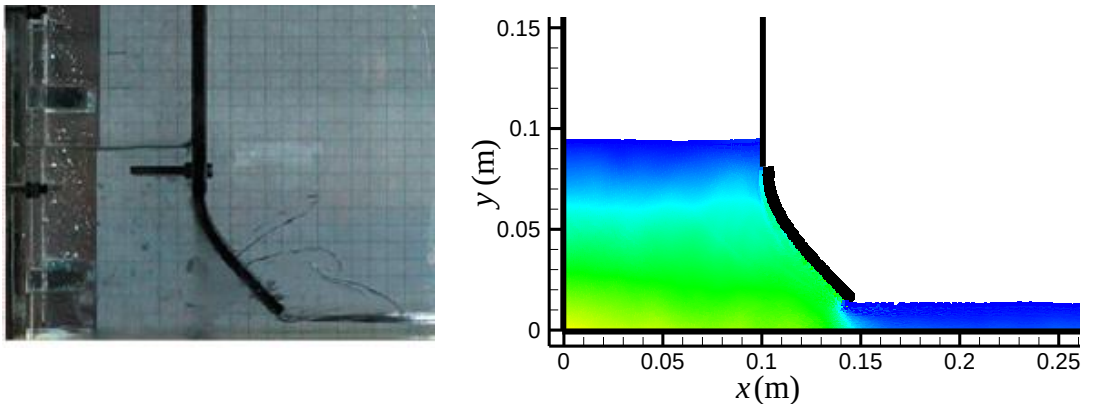

(b) $t = 0.292$ s

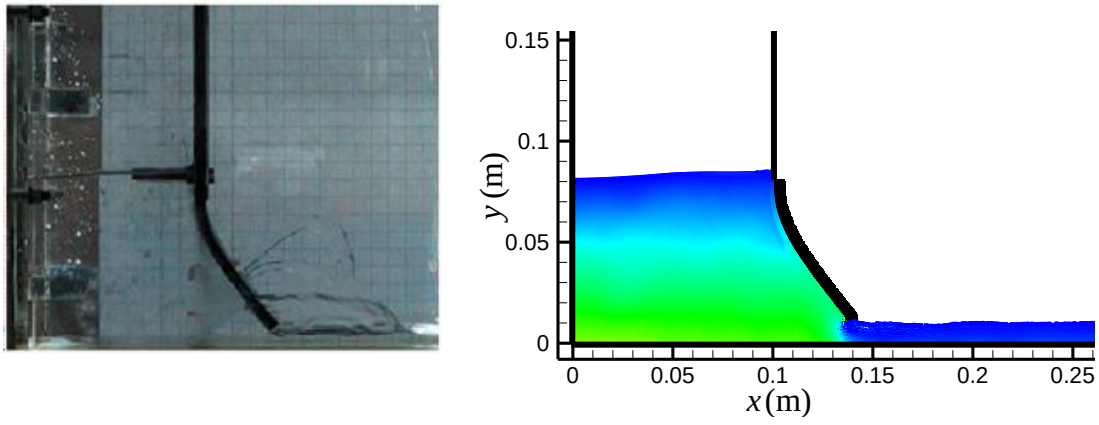

(c) $t = 0.405$ s

Fig. 3. Comparisons of the deformation progress of plate between laboratory photograph (Antoci et al., 2007) (left) and SPH particle snapshots (right) (contours of water pressure) at different time.

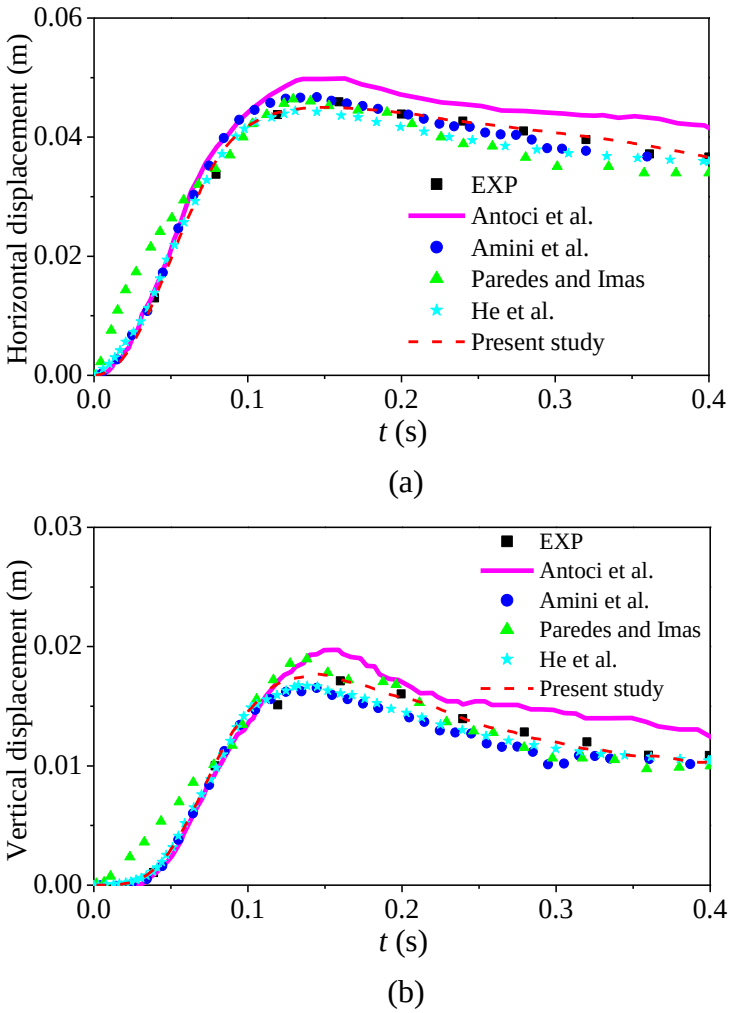

Fig. 4. Comparisons of time histories between different SPH results and experimental data: (a) horizontal displacement; (b) vertical displacement for the free end of the plate.

In order to evaluate the enhanced performance of the presented SPH method in detail，the convergence properties of the SPH results are examined in terms of the horizontal displacement for the free end of the plate. For this purpose, the time histories of horizontal displacement of SPH are presented in **Fig. 5(a)** with the different particle numbers N. **Fig. 5(b)** gives the convergence tests on horizontal displacement. It is shown in **Fig. 5(a)** that the results become closer to the experimental value with the increasing of particle numbers. The results of **Fig.5(b)** indicate that the errors of the horizontal displacement decrease with the decreasing particle size, and demonstrate a roughly first-order convergence ratio. It has been recorded that the CPU time (Intel i7 3.4 GHz with RAM 8 GB) of present simulation is 168.7 s with $N = 2304$, 2654.5 s with $N = 14395$ and 5952.2 s with $N = 28217$, respectively.

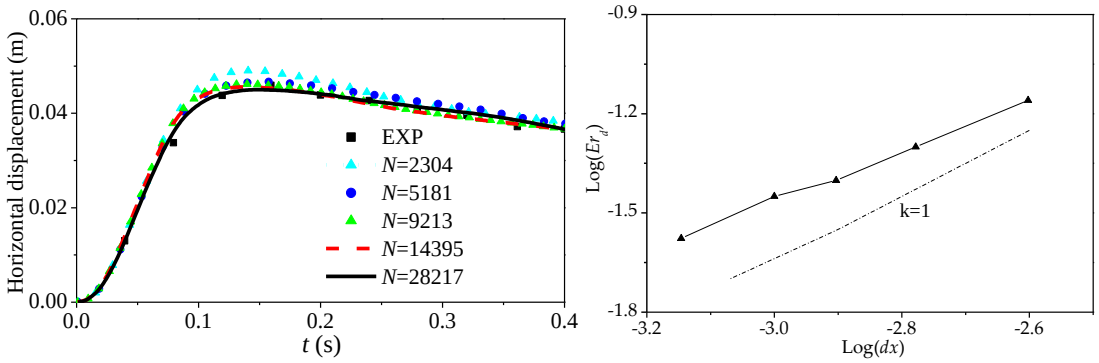

(a) (b)

Fig. 5. The convergence test of the deformation progress of plate: (a) The time histories of horizontal displacement with different particle numbers; (b) Error of numerical results corresponding to different particle sizes.

During the fluid-structure interaction, the transmission of the fluid energy to the structure is a notable problem (Amini et al., 2014). To investigate the conservation of energy for the presented SPH model, **Fig. 6** shows the time history of whole energy of the system during the simulation. It is noted that the energy losses on other fixed walls have been removed in **Fig. 6**. It shows that the presented SPH model cannot satisfy the energy conservation completely, which means there exist a few energy losses at the interface domain. This situation can be improved, as the energy losses will decrease with the increasing particle number

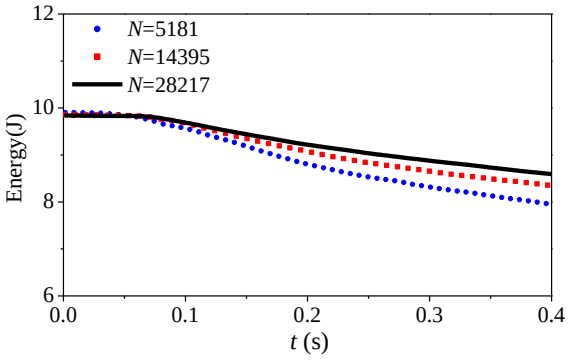

Fig. 6. Time history of the energy changes with different SPH particle numbers.

According to the numerical results compared with other fluid-solid interaction treatment method employed, the presented interface treatment algorithm in SPH is effective and gets better performance.

5. Numerical results and analysis

In order to investigate the effectiveness of the proposed SPH method for the wave-ice interaction simulation, two typical tests are included, one is the wave-induced kinematic response and the other one is the flexure of an ice floe. Quantitative comparison with experimental data shows that the proposed SPH algorithm has good performance.

5.1. Validation of numerical wave basin

In this part, the SPH method is applied to simulate a numerical wave basin. The wave tank is 20 m long, the initial still water depth is $d = 0.5$ m. The incident wave height and wave period are $H = 0.12$ m and $T = 1.2$ s respectively. Two measurement points G_1 and G_2 are fixed to monitor the wave profile on time histories, which are located at $x = 7.0$ m and $x = 10.0$ m from the left end of the wave basin respectively. The schematic of this wave basin is shown in **Fig. 7.**

Regular waves can be generated by using a piston wavemaker based on the linear theory. Similar to the Gotoh et al. (2004) and Gao et al. (2012), the motions of the wavemaker can be defined as

$$\begin{cases} S(t) = \dfrac{x_0}{2}\sin(\omega t) \\ U(t) = \dfrac{x_0\omega}{2}\cos(\omega t) \end{cases} \tag{26}$$

where $S(t)$ and $U(t)$ are the displacement and velocity of the wave maker, respectively. Besides, x_0 and ω are the motion amplitude and frequency of the wave maker. $x_0 = H / Q$, Q is the transfer function, which can be presented as

$$Q = \frac{4\sinh^2 kd}{2kd + \sinh 2kd} \tag{27}$$

An artificial sponge layer is fixed at the right end of the flume to prevent the undesirable wave reflections. In the damping zone, the final velocity of fluid particle is corrected by a velocity damping coefficient (μ) at the end of each time step. Following Wei and Kirby (1995) and Li et al. (2012), the damping coefficient of velocity attenuation (μ) can be written as

$$\mu = 1 - c_a \frac{\exp\left[\left(\frac{|x - x_s|}{l_s}\right)^{n_a}\right] - 1}{\exp(1) - 1}, \quad x_s \le x \le x_s + l_s \tag{28}$$

where x_s and l_s are the starting position and length of the damping region, respectively, c_a and n_a are the empirical damping coefficients which can be determined by the numerical test. $c_a = 0.1$ and $n_a = 6$ are adopted in this paper.

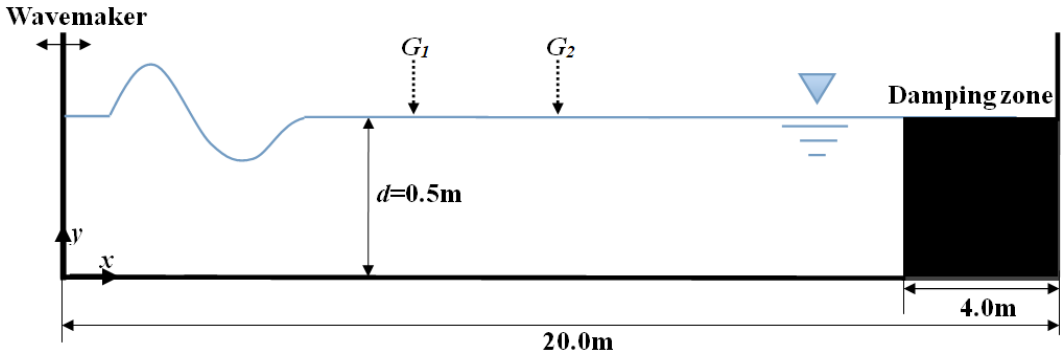

Fig. 7. Schematic setup of the numerical wave tank.

Fig. 8 shows the comparison of the time history of the wave profiles with the analytical results obtained from the second-order Stokes waves (Madsen, 1971) at the two measuring points. According to the results in **Fig. 8**, as the particle number increases, the difference between numerical results and the analytical solution becomes smaller. This has clearly evidenced the convergence of numerical results in spatial domains. Furthermore, the free surfaces predicted by the SPH approach shows a very good agreement with the analytical solution when particle number $N = 100000$, although there still exists some little differences in the area of wave crest.

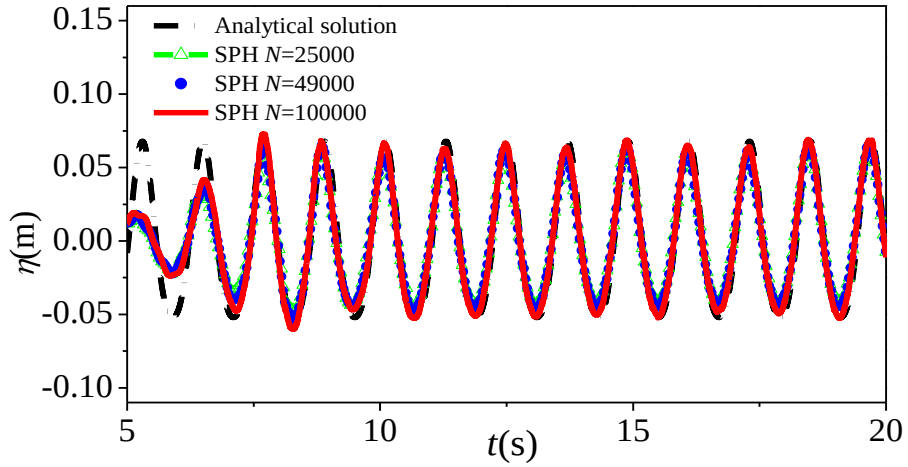

(a)

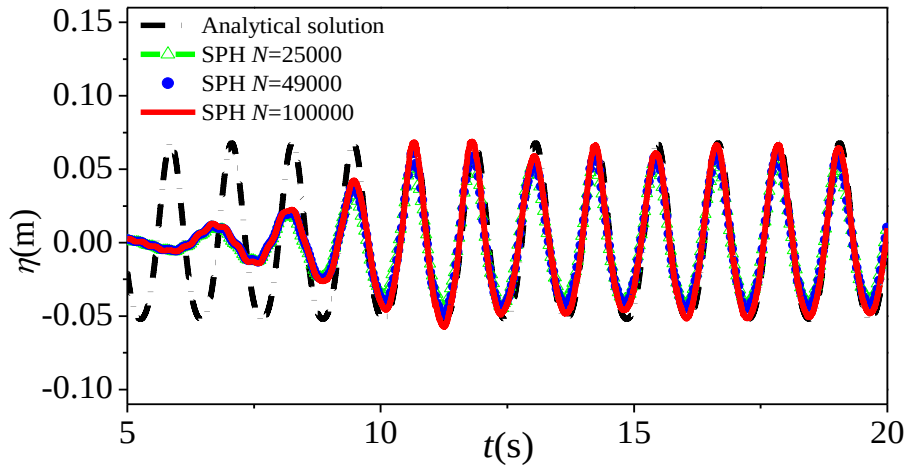

(b)

Fig. 8. Comparisons of wave surface profiles between analytical and SPH results at two measuring points: (a) $x = 7.0$ m; and (b) $x = 10.0$ m.

In order to study the performance of the wave damping zone on the wave propagation, **Fig. 9** shows the comparison between analytical solution and numerical results at the last two periods of wave propagation at the measure point $x = 10.0$ m. The results of the presented SPH show a slight underestimation of the wave crest and trough. The average relative errors Er_a are given in **Fig. 10(a)**. Besides, **Fig. 10(b)** shows the average phase difference φ_d at the wave crest and trough between the analytical solutions and numerical results. According to the results of **Fig. 10**, with a decrease in the particle size (or an increase in the particle number), the errors between the analytical and SPH results decrease accordingly.

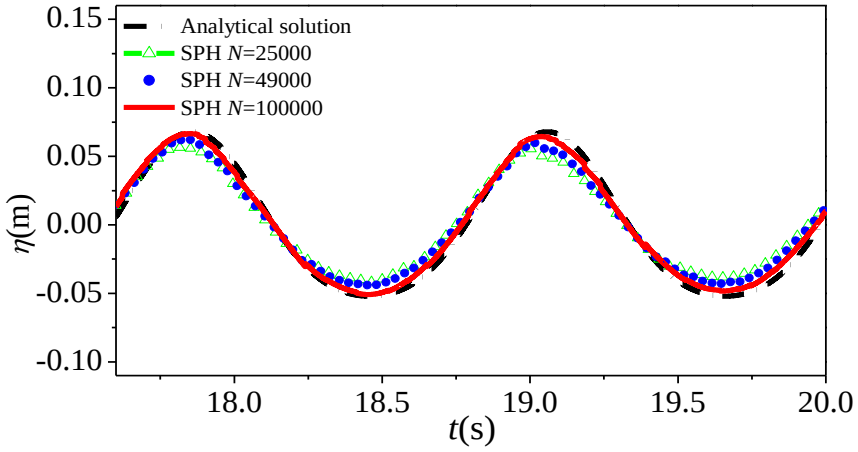

Fig. 9. Comparisons of wave surface profiles between analytical and SPH results with

different particle numbers for the last two wave periods at $x = 10.0$ m.

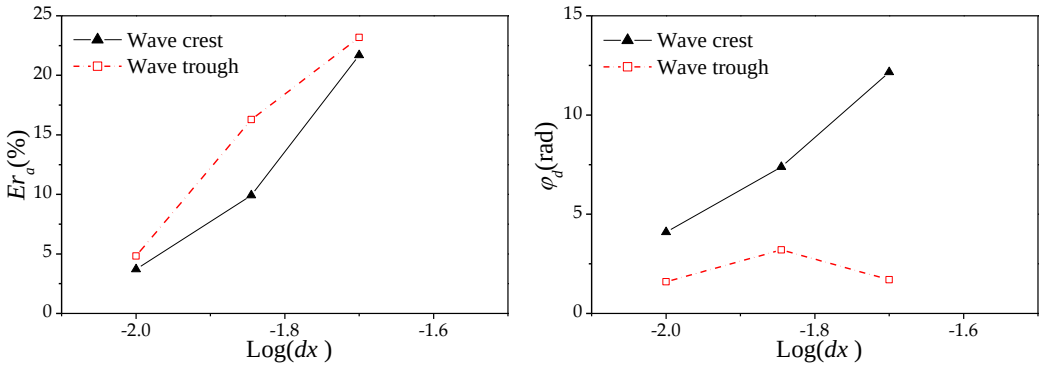

Fig. 10. Comparisons of errors between analytical and SPH results with different particle numbers for the last two periods: (a) average relative errors of wave peak and trough; (b) average phase difference at wave crest and trough.

In order to investigate the wave amplitude and phase shifting, the discrete Fourier transform (DFT) has been adopted for the last two periods of the wave profiles. DFT convert the time series $s(n)$ of wave surface profiles to its Fourier components $S(f)$:

$$S(f) = \sum_{n=1}^{N} s(n) \exp(-2\pi i f t_n) \tag{29}$$

where $f = 1/T$ is the wave frequency, N is the total number of the selected time series and $t_n = ndt$.

The wave amplitude A_f and wave phase ϕ_f can be obtained separately by

$$A_f = \frac{2}{N}|S(f)|, \quad \phi_f = \tan^{-1}\left(\frac{\mathrm{Im\,ag}[S(f)]}{\mathrm{Re\,al}[S(f)]}\right) \tag{30}$$

According to the SPH results of wave basin simulation in the case of particle number $N = 100000$, the estimated wave amplitude by the DFT method yields 0.056 m and the wave phase is -74.03° . In contrast, the corresponding wave amplitude and wave phase obtained by the DFT method is 0.06 m and -77.54° respectively for analytical wave surface profiles. The relative errors between analytical solution and numerical result are about 6.67% and 4.53% respectively.

5.2. Response of small sea ice floes in regular waves

In this section, a numerical investigation is presented to study the kinematic response of sea ice floes in waves. The surge, heave displacement and the corresponding of

velocity are analyzed by using the presented SPH model. The numerical results are compared against available experimental data. The experiment on kinematics of sea ice floes in regular waves was conducted by Mcgovern and Bai (2014). In their study, the paraffin wax of density $\rho = 890.0$ kg/m^{-3} was used to construct the ice floe model. The initial model is shown in **Fig. 11.** The model ice floe is 30 cm long and 5 cm thick. The model ice floe has the elastic modulus $E = 2.0$ GPa. In this case, the initial particle size is 0.0125 m.

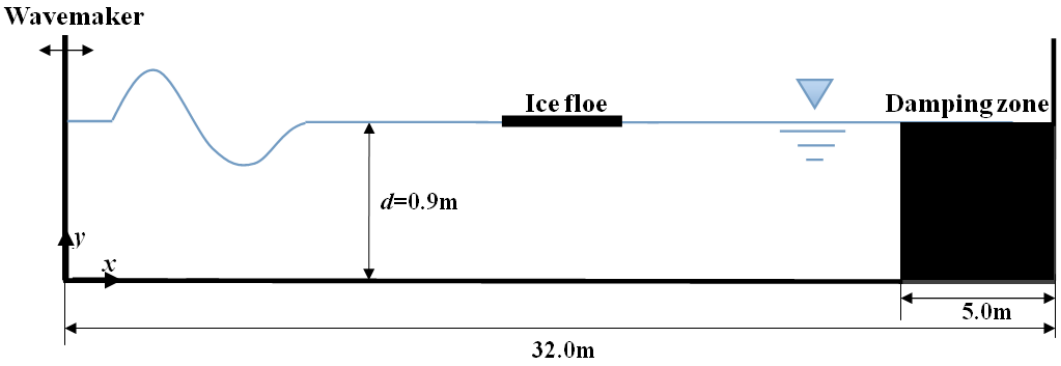

Fig. 11. Schematic setup of the model ice floe in the regular wave.

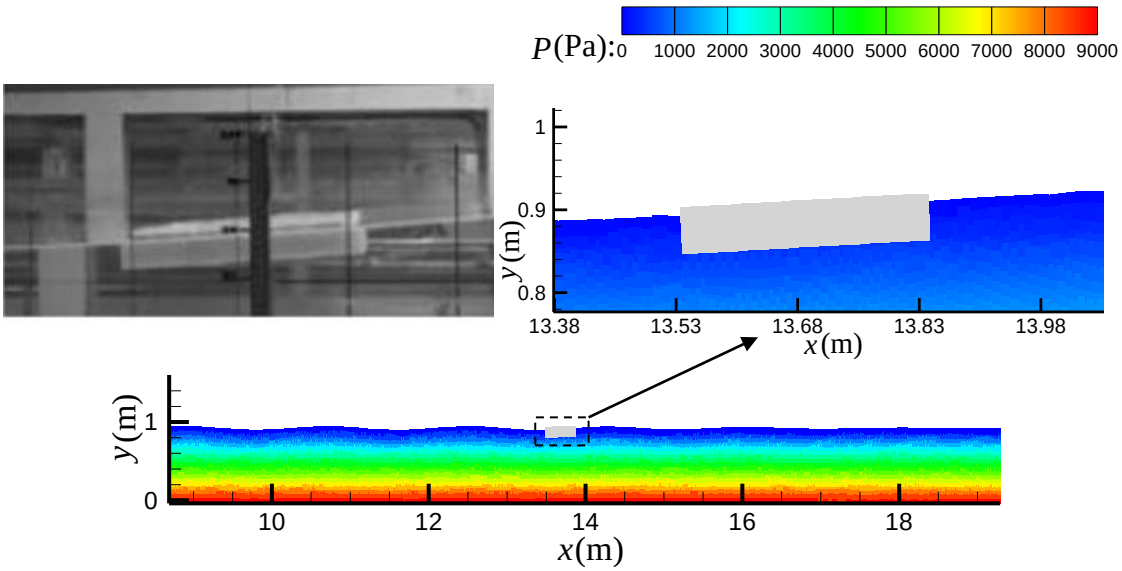

(a) $t = 19.6$ s

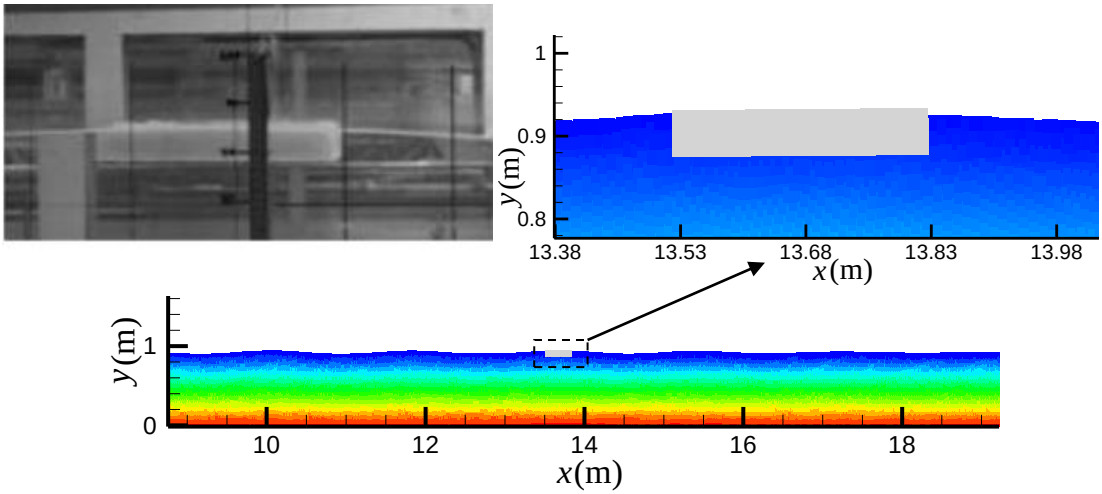

(b) $t = 20.3$ s

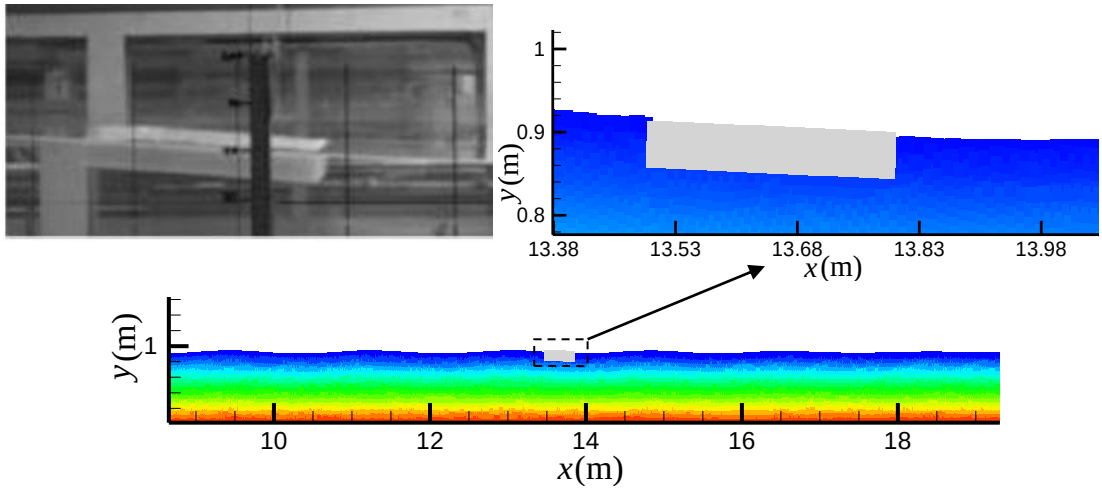

(c) $t = 21.0$ s

Fig. 12. Comparisons of the motion progress of model ice floe between laboratory photograph (Mcgovern and Bai, 2014) (left) and SPH particle snapshots (right) (contours of wave pressure) at different time.

Fig. 12 shows a series of comparisons between the numerical results and experimental photographs for the motion progress of the model ice floe. The experimental data are obtained from Mcgovern and Bai (2014) with wavelength $\lambda = 1.8$ m and wave height $H = 0.05$ m at different time. According to the results of **Fig. 12(a)**, the ice floe rises and moves forward obviously under the action of wave force. Then, the ice floe reaches the maximum rising position under the wave crest, as shown in **Fig. 12(b)**. After that, the ice floe moves backwards and drops down as the wave falls, which is shown in **Fig. 12(c)**. Generally, the agreement between numerical and experimental results is quite satisfactory.

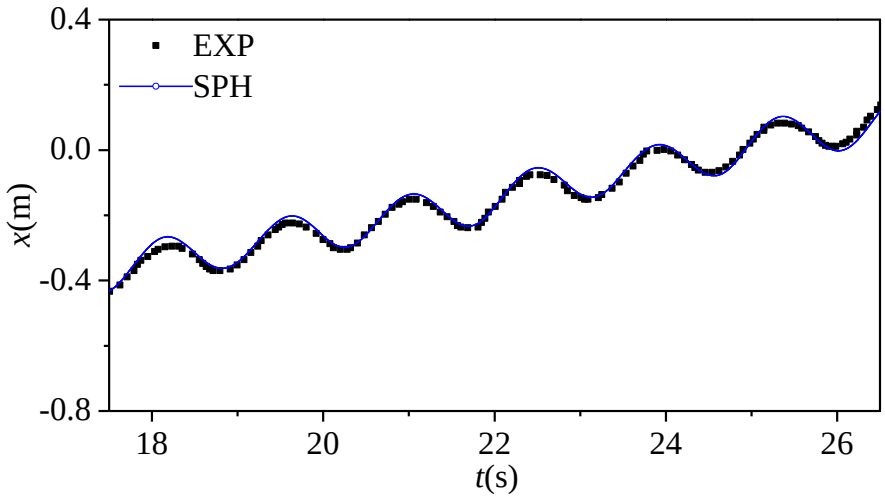

(a) Surge displacement

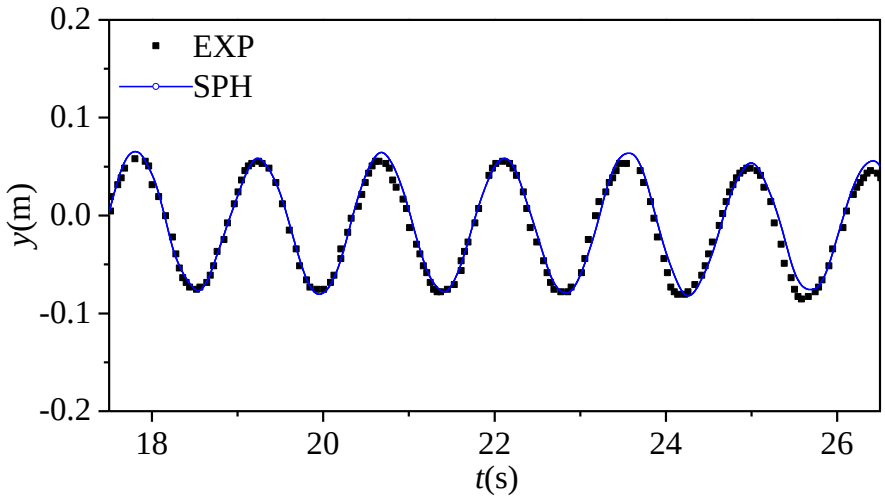

(b) Heave displacement

Fig. 13. Comparisons of time histories of ice floe motion in regular wave between SPH results and experimental data: (a) surge in x direction and (b) heave in y direction.

In order to quantify the numerical results of the presented SPH, **Fig. 13** shows the comparison of the model ice floe displacements in the x and y directions between the SPH results and experimental data. The tested cases just consider the steady state with the wave length $\lambda = 3$ m and wave height $H = 0.148$ m. By examining **Fig. 13(a)**, the ice floe can move forward step by step, and there are some oscillation motions added in the x direction during each wave period. According to **Fig. 13(b)**, the ice floe moves up and down with the wave in the y direction periodically. The numerical results of SPH coincide reasonably with the experimental data in Mcgovern and Bai (2014) for the surge and heave motions, in spite of the unavoidable discrepancies. This provides a certain indication that the proposed SPH procedure can simulate the

wave-induced kinematic response of a small ice floe effectively and acquire accurate numerical results.

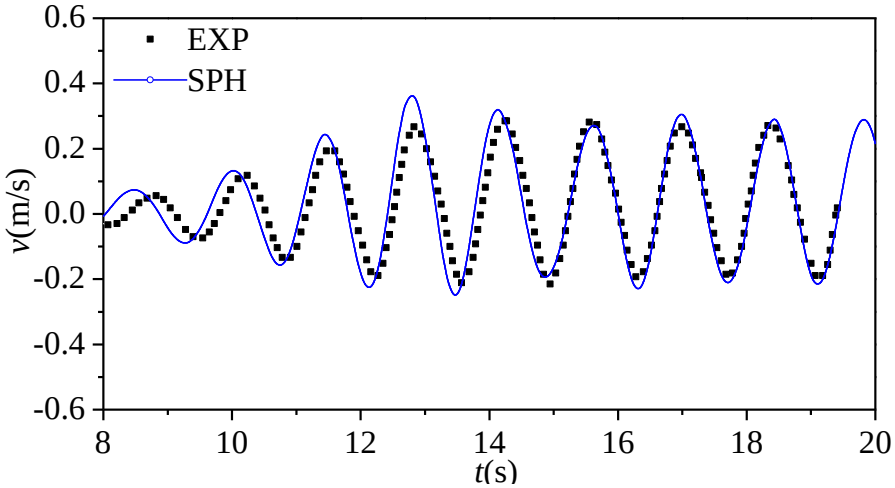

(a)

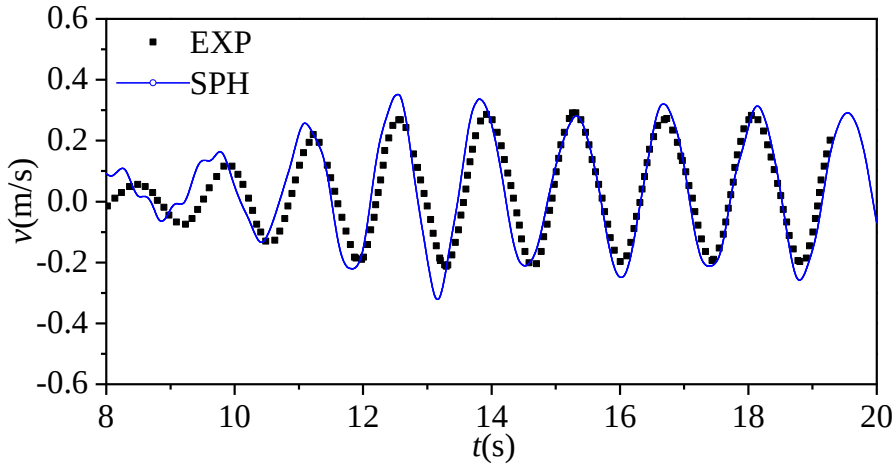

(b)

Fig. 14. Comparisons of the ice floe velocity in regular wave of $\lambda = 3$ m, and $H = 0.132$ m between SPH results and experimental data: (a) x direction; (b) y direction.

The velocity of ice floe is the noteworthy quantity in the calculation of wave induced motion of an ice floe. In this part, an investigation of the velocity of ice floe is conducted to verify the accuracy of the computed results. **Fig. 14** gives the time history comparison of the ice floe velocities between SPH results and the experimental data in the x and y directions, respectively. The surge velocity in the positive direction is larger than that in the negative direction, which corresponds to the trend of surge displacement in Fig. 12(a). During the first few periods, the difference between the numerical results and the experimental data is relatively large. However

when the steady state is reached after about $t=14$ s, the trend of x and y velocities predicted by the SPH method shows a good agreement with the experimental data.

In addition, the drift velocity is also an important quantity for ice motion. For a pure wave motion in fluid dynamics, the Stokes drift velocity is the average velocity. The equation of the drift velocity based on the Stokes theory can be given as follows:

$$V_d = \frac{ga^2k^2 \cosh 2k(H+\mathrm{y})}{f \sinh 2kH} \tag{31}$$

where k, a and f are the wave number, wave amplitude and wave frequency, respectively.

According to Eq. (31), the drift velocity obtained by the Stokes theory is a quadratic function of the wave steepness ka. In this case, the wavelength is a constant at $\lambda=1.8$ m and the corresponding wave height and ka value can be found in Mcgovern and Bai (2014). In numerical results, the period-averaged Stokes drift velocity V_d is obtained by searching the horizontal displacement between two peaks and dividing by the wave period T. Then the corresponding values for five wave cycles during a quasi-steady state are taken and averaged.

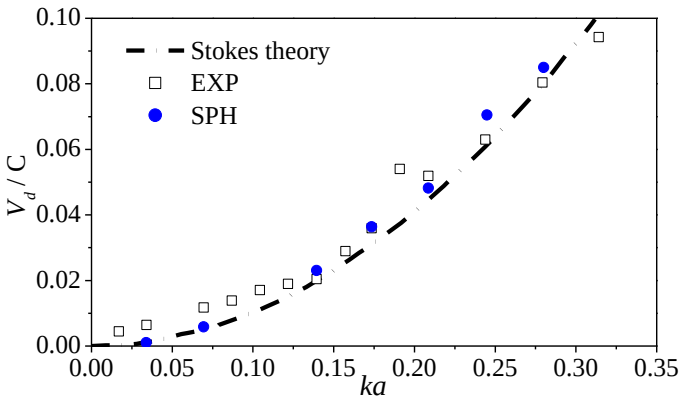

Fig. 15. Comparisons of drift velocity for the model ice floe among SPH results, experimental data and analytical solution.

Fig. 15 shows the comparisons of drift velocity for the ice floe between the SPH results, experimental data (Mcgovern and Bai, 2014) and analytical solutions calculated by the Stokes theory. The drift velocity is normalized by the wave celerity C, which is a function of ka. As shown in **Fig. 15,** the numerical and experimental values are slightly larger than the theoretical results, but they are generally all in good agreement, which is similar to the findings in Bai et al. (2017).

5.3. Wave-induced flexure of an Ice Floe

In this part, the flexural deformation of ice floe caused by regular wave impact is given The experimental investigation of wave-induced flexure of a sea ice floe was conducted by Meylan et al. (2014), in which a thin plastic plate was applied to model the ice floe. The general layout of initial calculation model is shown in **Fig. 16**. The model ice floe has density $\rho = 500.0$ kg/m^3, thickness $h = 10$ mm, length $l = 1.0$ m and the elastic modulus $E = 500$ MPa, which are same with that in the model test by Meylan et al. (2014). In this case, the initial particle size is 0.015 m. In addition, the model ice floe is moored loosely. The mooring line system is taken as a light spring model and the value of mooring force can be written as

$$\boldsymbol{F}_{moor} = \begin{cases} k\left(l_t - l_{t0}\right) & l_t - l_{t0} > 0 \\ 0 & else \end{cases} \tag{32}$$

where k is the coefficient of elasticity of mooring line. l_t and l_{t0} are the transient length and the initial mooring line length, respectively.

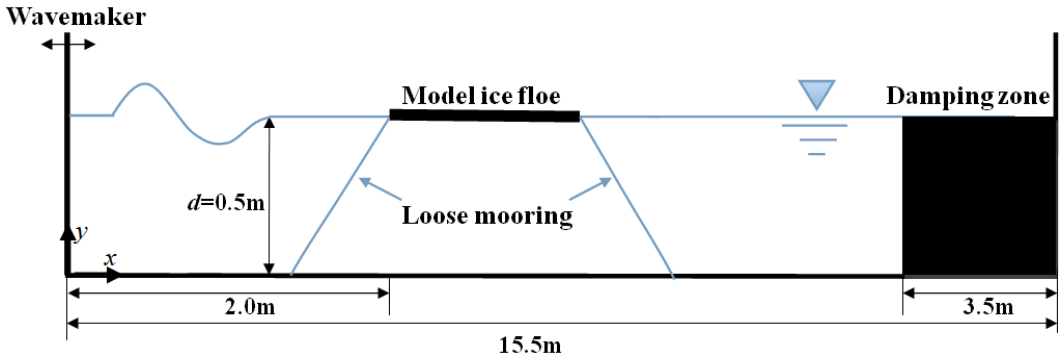

Fig. 16. The general layout of computational model of wave-induced flexure of an ice floe.

(a1) The snapshot in laboratory

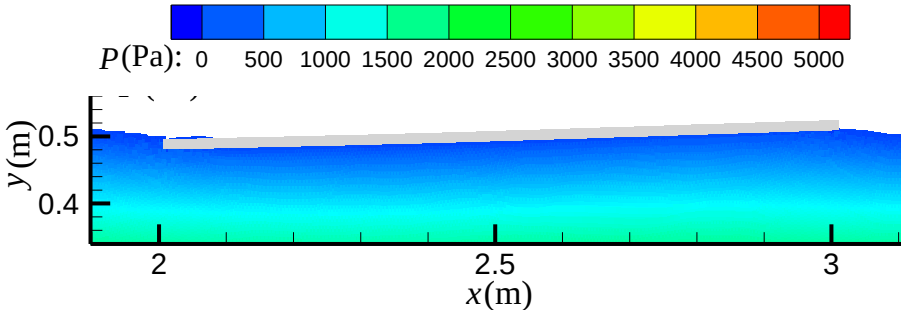

(a2) SPH

(a)

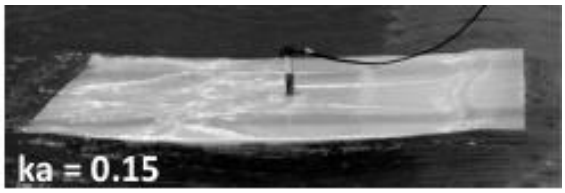

(b1) The snapshot in laboratory

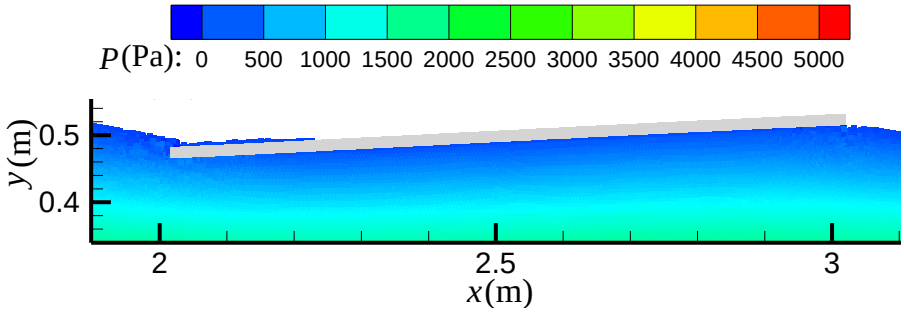

(b2) SPH

(b)

Fig. 17. Comparisons of the model ice floe overwash between the experimental results (upper snapshots) and the SPH results (lower snapshots) for wavelength $\lambda = 1$ m: (a) Wave stepness $ka = 0.1$; (b) Wave stepness $ka = 0.15$.

Fig. 17 shows the comparisons of the mode ice floe overwash with different wave steepness between the experiment snapshots from Meylan et al. (2014) and numerical results of the presented SPH. The model ice floe exhibits obvious bending deformation according to the results in **Fig. 17**. The overwash of the mode ice floe at the left end can be captured obviously in numerical results, although there exists a little difference with the experimental snapshots, especially for the case of wave stepness $ka = 0.15$, where k is the wave number and a is the wave amplitude.

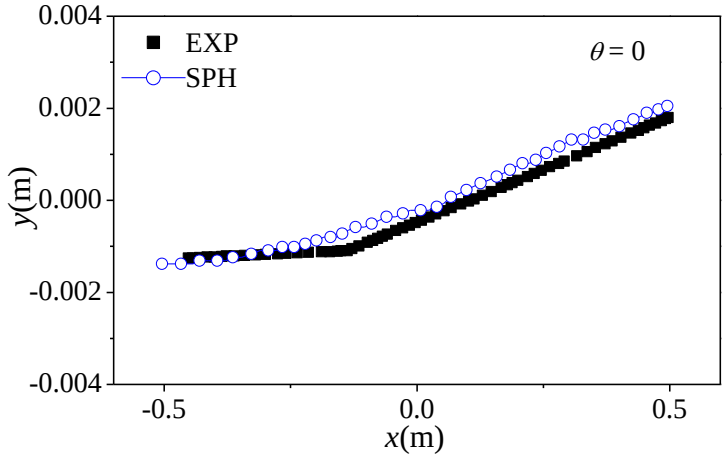
EXP
SPH
θ = 0
0.004
0.002
0.000
-0.002
-0.004
y(m)
-0.5
0.0
0.5
x(m)

(a)

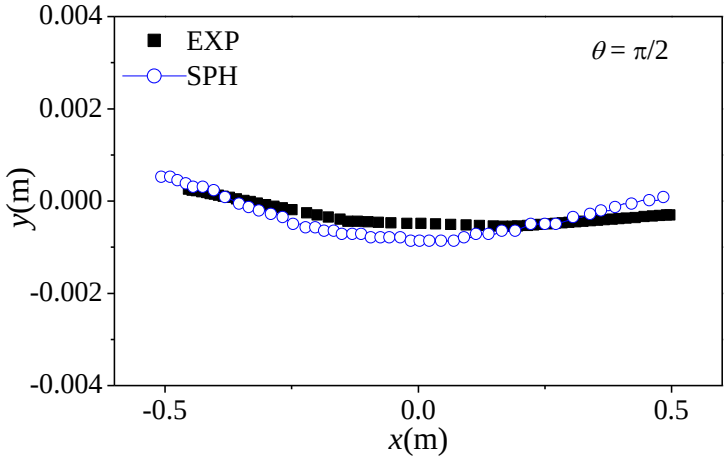
EXP
SPH
θ = π/2
0.004
0.002
0.000
-0.002
-0.004
y(m)
-0.5
0.0
0.5
x(m)

(b)

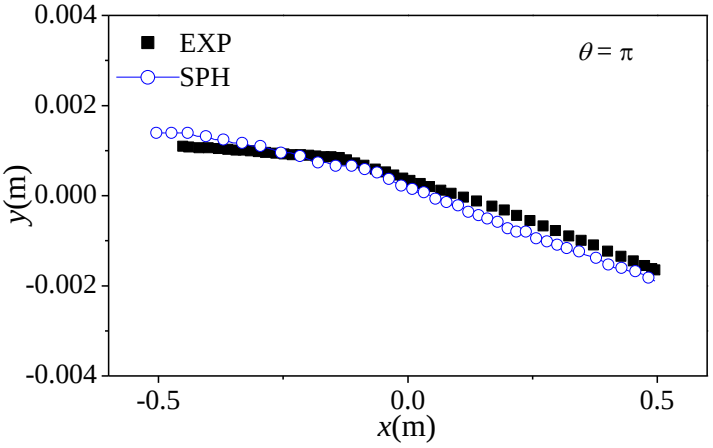
EXP
SPH
θ = π
0.004
0.002
0.000
-0.002
-0.004
y(m)
-0.5
0.0
0.5
x(m)

(c)

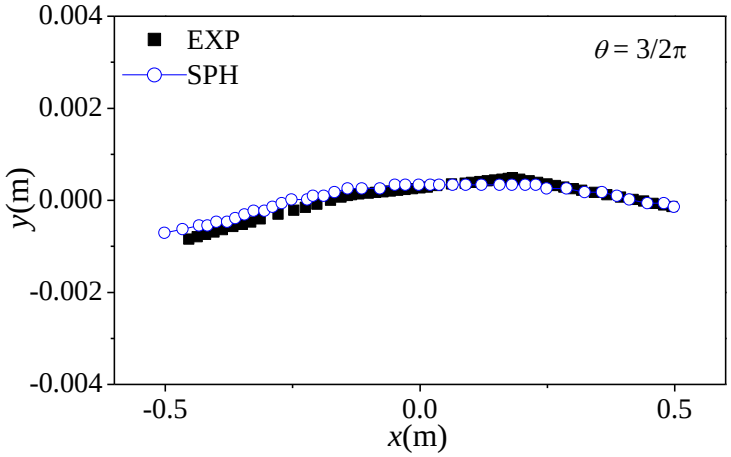

(d)

Fig. 18. Comparisons of flexure of the ice floe in regular wave between SPH results and experimental data when wave steepness is 0.04: (a) $\theta = 0$; (b) $\theta = \pi / 2$; (c) $\theta = \pi$; (d) $\theta = 3/2\pi$.

Fig. 18 gives the comparisons of bending motion of the model ice floe between the presented SPH and experimental data for a period 0.6 s in which the steepness is 0.04 and the θ indicates the wave phase. According to **Fig. 18**, the model ice floe has four typical bending patterns during one wave period. In addition, the flexure motions obtained by the SPH method are generally in reasonable agreement with the experimental results although there are some differences. The SPH results show more significant bending deformation than that of experimental data, especially for the case of $\theta = \pi/2$. One probable reason is that the SPH results are based on two-dimensional case while the experiment data is in three-dimension.

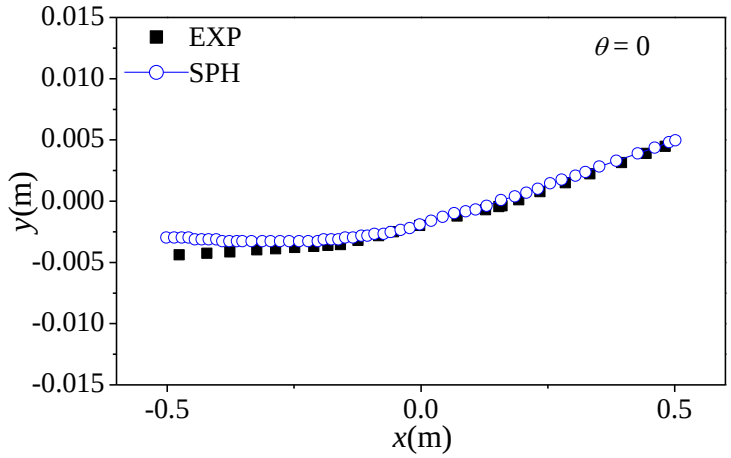

(a)

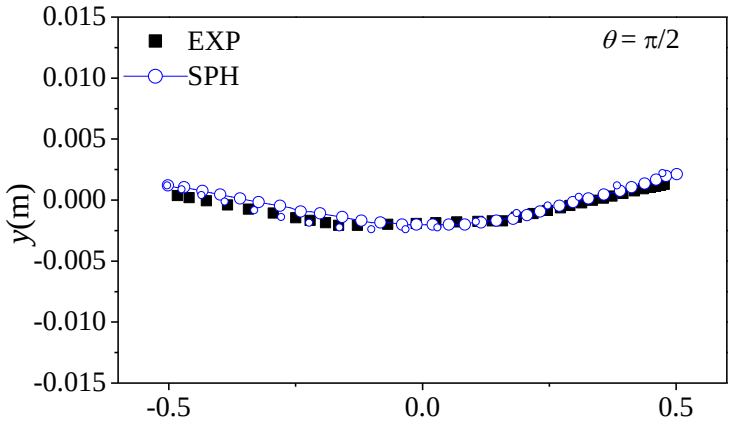

(b)

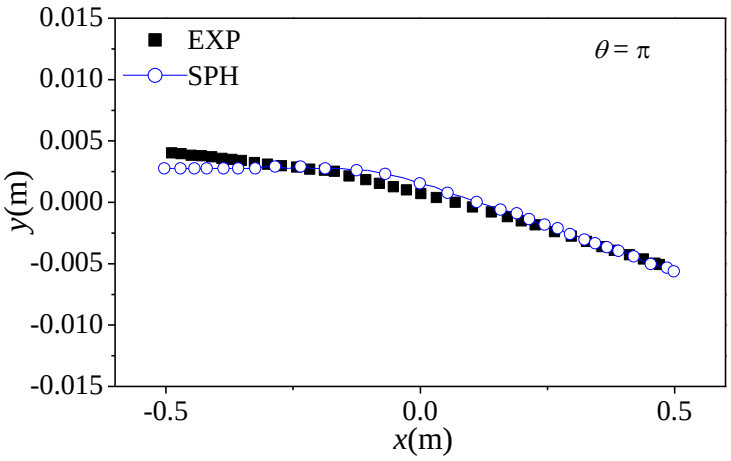

(c)

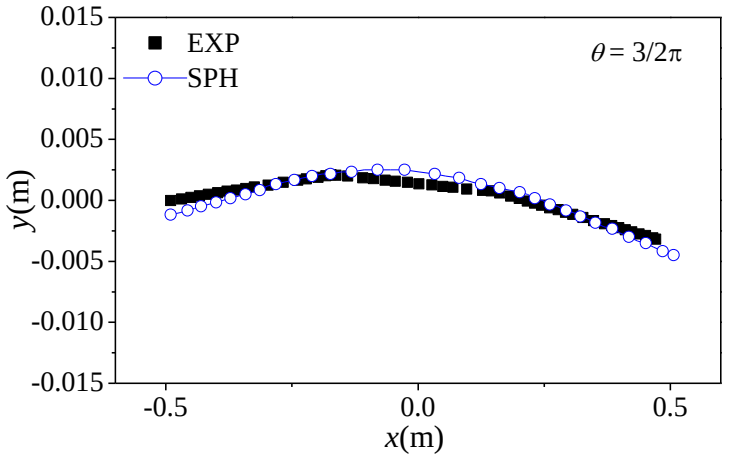

(d)

Fig. 19. Comparisons of flexure of the model ice floe between SPH results and experimental data in regular wave with wave steepness of 0.15: (a) $\theta = 0$; (b) $\theta = \pi/2$; (c) $\theta = \pi$; (d) $\theta = 3/2\pi$.

In order to validate the numerical model further, **Fig. 19** gives the equivalent comparison as **Fig. 18** for the wave steepness of 0.15. According to the results of **Fig.**

19, the presented SPH model can give satisfactory results for predicting wave-induced flexure of ice floe when the wave steepness increases. The flexural displacement of ice floe increases with the increasing of the wave steepness. According the results of **Fig. 18** and **Fig. 19**, the displacement of the ice floe flexure predicted by the presented SPH is slightly larger than the one of the experimental data in **Fig. 19**. There exist some obvious differences of the bending deformation on both ends of the ice floe between the SPH results and the experimental values. One important reason is the uncertainty of the mooring force on both ends of the ice floe.

During the flexural motion, the ice floe will get the biggest flexural displacement. The maximum flexural displacement of the ice floe is a noteworthy quantity and reflects the response amplitude of the ice floe caused by wave impact. So the biggest flexural displacement in the middle of the ice floe is investigated in **Fig. 20**. In this case, the maximum flexural displacements in the middle of the ice floe changes with different length l and wave height H by the presented SPH method. The maximum flexural displacements can increase linearly with wave height. In addition, the larger length l of ice floe can cause greater flexural displacements with the same wave height.

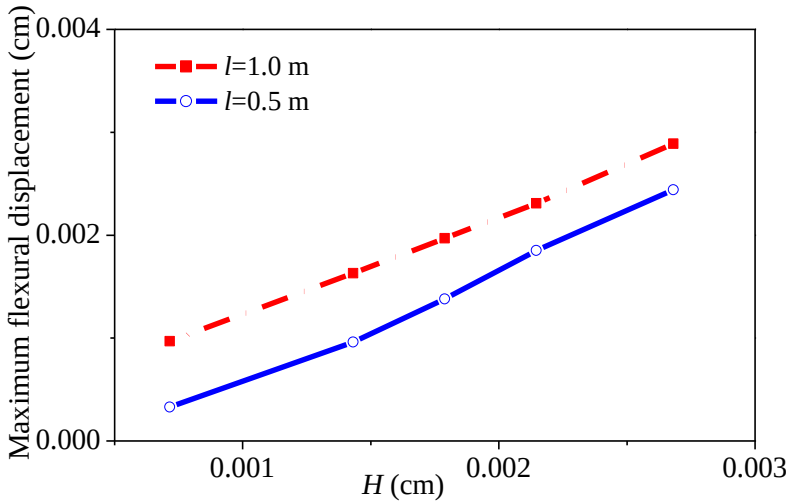

Fig. 20. Comparisons of maximum flexural displacements in middle of ice floe predicted by the presented SPH with different floe length l and wave height H .

Conclusion

The SPH model including a simple and effective fluid-ice interaction algorithm is presented to simulate the wave-ice interaction. The proposed treatment scheme has the advantages of computational simplicity and avoiding the issues in other interface

methods, such as the requirement to calculate the normal direction of the interface surface or interface particles. The proposed interface algorithm is validated through the elastic deformation of a plate subjected to the water pressure. Then the SPH model is applied to study two typical cases of wave-ice interaction, including the kinematics of a small ice floe in waves and the wave-induced flexure of an ice floe. According to the comparisons between the numerical results and the experimental data, the performance of the presented SPH is found to be satisfactory in view of accuracy and stability, although there still have some kinds of differences. Future work is needed to improve the method to simulate more practical and complex water wave-ice interactions, such as the wave-induced ice floe breakups.

Acknowledgements

This work is sponsored by the National Natural Science Foundation of China (Nos. 51739001, 51279041, 51379051 and 51639004), Foundational Research Funds for the Central Universities (Nos. HEUCF170104 and HEUCDZ1202), Defense Pre Research Funds Program (Nos. 9140A14020712CB01158) and China Scholarship Council. The third author also thanks the Chang Jiang Visiting Chair Professorship scheme of the Chinese Ministry of Education, hosted by HEU. The authors are grateful to Songdong Shao at the University of Sheffield for his helpful feedbacks during the revision of the manuscript.

References

Adami, S., Hu, X.Y., Adams, N.A., 2012. A generalized wall boundary condition for smoothed particle hydrodynamics. J. Comput. Phys. 231(21), 7057-7075.

Amini, Y., Emdad, H., Farid, M., 2011. A new model to solve fluid–hypo-elastic solid interaction using the smoothed particle hydrodynamics (SPH) method. Eur. J. Mech. B-Fluid. 30(2), 184-194.

Amini, Y., Emdad, H., Farid, M., 2014. An accurate model for numerical prediction of piezoelectric energy harvesting from fluid structure interaction problems. Smart Mater. Struct. 23(9), 095034.

Antoci, C., Gallati, M., Sibilla, S., 2006. SPH simulation of fluid-structure interaction problems. Seminars in Neonatology. 7(4), 275-281.

Antoci, C., Gallati, M., Sibilla, S., 2007. Numerical simulation of fluid–structure interaction by SPH. Comput. Struct. 85(11–14), 879-890.

Antuono, M., Colagrossi, A., Marrone, S., Molteni, D., 2010. Freesurface flows solved by means of sph schemes with numerical diffusive terms. Comput. Phys. commun. 181(3), 532-549.

Bai, W., Zhang, T., Mcgovern, D.J., 2017. Response of small sea ice floes in regular waves: a comparison of numerical and experimental results. Ocean Eng. 129, 495-506.

Bennetts, L.G., Alberello, A., Meylan, M.H., Cavaliere, C., Babanin, A.V., Toffoli, A., 2015. An idealised experimental model of ocean surface wave transmission by an ice floe. Ocean Model. 96(14), 85-92.

Bui, H.H., Sako, K., Fukagawa, R., 2007. Numerical simulation of soil–water interaction using smoothed particle hydrodynamics (SPH) method. J. Terramechanics 44(5), 339-346.

Cleary, P. and Prakash, M., 2004. Discrete-element modelling and smoothed particle hydrodynamics: Potential in the environmental sciences. Philos. Trans. R. Soc. London, Ser. A. 362(1822), 2003-2030.

Colagrossi, A., Antuono, M., Le Touzé, D., 2009. Theoretical considerations on the free surface role in the SPH model. Phys. Rev. E. 79 (5), 1-13. 056701.

Francis, O.P., Panteleev, G.G., Atkinson, D.E., 2011. Ocean wave conditions in the chukchi sea from satellite and in situ observations. Geophys. Res. Lett. 38(24), 24610.

Gao, R., Ren, B., Wang, G., Wang, Y., 2012. Numerical modelling of regular wave slamming on subface of open-piled structures with the corrected sph method. Appl. Ocean Res. 34, 173-186.

Gotoh, H., Shao, S., Memita, T., 2004. SPH-LES model for numerical investigation of wave interaction with partially immersed breakwater. Coast. Eng. J. 46(1), 39-63.

Gray, J.P., Monaghan, J.J., Swift, R.P., 2001. SPH elastic dynamics. Comput. Methods Appl. Mech. Eng. 190(49-50), 6641-6662.

He, J.D., Tofighi, N., Yildiz, M., Lei, J.M., Suleman, A., 2017. A coupled wc-tl sph method for simulation of hydroelastic problems. Int. J. Comput. Fluid D. 31(3), 174-187.

Khayyer, A., Gotoh, H., Shao, S., 2008. Corrected incompressible SPH method for accurate water surface tracking in breaking waves. Coast. Eng. 55(3), 236-250.

Kohout, A.L., Meylan, M.H., 2008. An elastic plate model for wave attenuation and ice floe breaking in the marginal ice zone. J. Geophys. Res-ceans. 113(C9), 159-166.

Kohout, A.L., Williams, M.J.M., Toyota, T., Lieser, J., Hutchings, J., 2016. In situ observations of wave-induced sea ice breakup. Deep-Sea Res. Pt II. 131, 22-27.

Li, J., Liu, H., Gong, K., Tan, S.K., Shao, S., 2012. SPH modeling of solitary wave fissions over uneven bottoms. Coast. Eng. 60, 261-275.

Libersky, L.D., Petschek A.G., 1991. Smoothed particle hydrodynamics with strength of materials. In Proceedings of the Next Free Lagrange Conference, Trease H, Friits J, Crowley W (eds). Springer: New York , 395, 248-257.

Libersky, L.D., Petschek A.G., Carney T.C., Hipp J.R., Allahdadi F.A., 1993. High strain Lagrangian hydrodynamics: A three-dimensional SPH code for dynamic material response. J. Comput. Phys. 109(1), 67-75.

Madsen, O.S., 1971. On the generation of long waves. J. Geophys. Res. 76(36), 8672-8683.

Ma, Q.W., 2008. A new meshless interpolation scheme for MLPG_R method. CMES-Comp Model. Eng. 23(2), 75-89.

Mcgovern, D.J., Bai, W., 2014. Experimental study on kinematics of sea ice floes in regular waves. Cold Reg. Sci. Technol. 103(103), 15-30.

Meylan, M.H., Bennetts, L.G., Cavaliere, C., Alberello, A., Toffoli, A., 2015. Experimental and theoretical models of wave-induced flexure of a sea ice floe. Phys. Fluids 27(4), L24610.

Meylan, M.H., Troffoli, A., Bennetts, L.G., Cavaliere, C., Alberello, A., Babanin, A.V. (2014). An experimental model of wave-induced motions of an ice floe. In Proceedings of the 19th Australasian Fluid Mechanics Conference, Melbourne, Australia, 8-11 December.

Monaghan, J.J., Lattanzio, J.C., 1985. A refined particle method for astrophysical problems. Astron. Astrophys. 149(149), 135-143.

Monaghan, J.J., 1992. Smoothed particle hydrodynamics. Annu. Rev. Astron. Astrophys. 30, 543-574.

Monaghan, J.J., 2000. SPH without a tensile instability. J. Comput. Phys. 159(2), 290-311.

Montiel, F., Squire, V.A., 2017. Modelling wave-induced sea ice break-up in the marginal ice zone. P. Roy. Soc. A-Math Phy. 473(2206), 20170258.

Morris, J., Fox, P., Zhu, Y., 1997. Modeling low Reynolds number incompressible flows using SPH. J. Comput. Phys. 136(1), 214-226.

Paredes, R., Imas, L., 2013. Application of multiphase SPH to Fluid Structure Interaction Problems. 9th International Spheric Workshop.

Randles, P., Libersky, L., 1996. Smoothed particle hydrodynamics: some recent improvements and applications. Comput. Methods Appl. Mech. Eng. 139(1), 375-408.

Ren, B., He, M., Dong, P., Wen, H., 2015. Nonlinear simulations of wave-induced motions of a freely floating body using wcsph method. Appl. Ocean Res. 50, 1-12.

Sakai, S., Hanai, K., 2002. Empirical formula of dispersion relation of waves in sea ice. In: Ice in the Environment: Proceedings of the 16th International Symposium on Ice, International Association of Hydraulic Engineering and Research, Dunedin, New Zealand, 2, 327-335.

Sergienko, O.V., 2010. Elastic response of floating glacier ice to impact of long-period ocean waves. J. Geophys. Res-earth. 115(F4), F04028.

Swegle, J., Hicks, D., Attaway, S., 1995. Smoothed particle hydrodynamics stability analysis. J. Comput. Phys. 116(1), 123-134.

Shao, S., Lo, E.Y.M., 2003. Incompressible SPH method for simulating newtonian and non-newtonian flows with a free surface. Adv. Water Resour. 26(7), 787-800.

Shao, S., 2010. Incompressible SPH flow model for wave interactions with porous media. Coast. Eng. 57(3), 304-316.

Skene, D. M., Bennetts, L. G., Meylan, M. H., Toffoli, A., 2015. Modelling water wave overwash of a thin floating plate. J. Fluid Mech. 777, R3.

Skene, D. M., Bennetts, L. G., Wright, M., Meylan, M. H., Maki, K. J., 2018. Water wave overwash of a step. J. Fluid Mech. 839, 293-312.

Squire, V.A., 2007. Of ocean waves and sea-ice revisited. Cold Reg. Sci. Technol. 49(2), 110-133.

Steele, M., 1992. Sea ice melting and floe geometry in a simple ice-ocean model. J. Geophys. Res-oceans. 97(C11), 17729-17738.

Stephenson, S.R., Smith, L.C., Agnew, J.A., 2011. Divergent long-term trajectories of human access to the arctic. Nat. Clim. Change 1(3), 156-160.

Timco, G.W., 2011. Isolated ice floe impacts. Cold Reg. Sci. Technol. 68(1), 35-48.

Toffoli, A., Bennetts, L.G., Meylan, M.H., Cavaliere, C., Alberello, A., Elsnab, J., Monty, J.P., 2015. Sea ice floes dissipate the energy of steep ocean waves. Geophys. Res. Lett. 42(20), 8547-8554.

Wendland, H., 1995. Piecewise polynomial, positive definite and compactly supported radial functions of minimal degree. Adv. Comput. Math. 4(1), 389-396.

Wei, G., Kirby, J.T., 1995. Time-dependent numerical code for extended Boussinesq equations. J. Waterw. Port Coast. 121, 251-261.

Williams, T.D., Bennetts, L.G., Dumont, D., Squire, V.A., Bertino, L., 2013. Wave-ice interactions in the marginal ice zone. Part 1: Theoretical foundations. Ocean Model. 71(Complete), 81-91.

Zhang, N.B., Zheng, X., Ma, Q.W., 2017. Updated smoothed particle hydrodynamics for simulating bending and compression failure progress of ice. Water 9(11), 882.

Zheng, X., Ma, Q.W., Duan, W.Y., 2014. Incompressible SPH method based on Rankine source solution for violent water wave simulation. J. Comput. Phys. 276, 291-314.